



OPEN

Machine learning molecular dynamics reveals the structural origin of the first sharp diffraction peak in high-density silica glasses

Keita Kobayashi^{1✉}, Masahiko Okumura^{1,4}, Hiroki Nakamura^{1,4}, Mitsuhiro Itakura^{1,4}, Masahiko Machida^{1,4}, Shingo Urata^{2,4} & Kentaro Suzuya^{3,4}

The first sharp diffraction peak (FSDP) in the total structure factor has long been regarded as a characteristic feature of medium-range order (MRO) in amorphous materials with a polyhedron network, and its underlying structural origin is a subject of ongoing debate. In this study, we utilized machine learning molecular dynamics (MLMD) simulations to explore the origin of FSDP in two typical high-density silica glasses: silica glass under pressure and permanently densified glass. Our MLMD simulations accurately reproduce the structural properties of high-density silica glasses observed in experiments, including changes in the FSDP intensity depending on the compression temperature. By analyzing the simulated silica glass structures, we uncover the structural origin responsible for the changes in the MRO at high density in terms of the periodicity between the ring centers and the shape of the rings. The reduction or enhancement of MRO in the high-density silica glasses can be attributed to how the rings deform under compression.

Silicon dioxide is an essential material used not only in glass manufacturing but also in the production of semiconductors^{1,2}. In addition to its industrial significance, silica glass is of great interest in fundamental research as an archetypal polyhedron network former³. One of the most fundamental issues of the polyhedron network forming materials is the origin of the first sharp diffraction peak (FSDP) in the total structure factor measured by neutron and X-ray diffraction (ND and XRD) experiments. The FSDP has been considered a signature of medium-range order (MRO) in disordered materials. Numerous models have been proposed to explain the relationship between the FSDP and the underlying atomic structures⁴. The periodicity of the quasi-crystalline^{5,6}, layered structures^{7,8}, cluster-like regions^{9,10}, and chemical ordering of the voids around cations^{11,12} have been explored as the structural origins of FSDP. The MRO and FSDP in amorphous materials have also been discussed in relation to their glass-forming ability^{13–16}. In the case of silica glass, the quasi-periodicity formed in the SiO_4 tetrahedral network is considered to induce FSDP in the total structure factor^{17–26}.

The FSDP is significantly affected by the density of silica glass^{24,27–31}. For example, it is well known that the FSDP heights of the permanently densified silica glass produced by cold compression^{27,28} and the silica glass under high pressure^{29,31} are significantly reduced, suggesting that the densification disrupts the MRO in the glasses. By contrast, Onodera et al.²⁴ recently reported unusual behavior of FSDP in high-density silica glass. They have shown that the permanently densified silica glass created via hot compression enhances the FSDP. Depending on the thermal treatment used for the formation of high-density silica glass, the FSDP exhibits the opposite behavior, which cannot be determined solely by the density. Thus, investigating high-density silica glass is crucial for understanding the origin of FSDP in disordered polyhedral network materials.

Reliable information in real space is essential for detailed investigations of the structural properties of disordered materials. However, XRD and ND experiments on noncrystalline materials can only provide one-dimensional structural information, such as total structure factors and their corresponding pair distribution functions. Therefore, computational methods, including the reverse Monte Carlo method, molecular dynamics

¹CCSE, Japan Atomic Energy Agency, Kashiwa, Chiba 277-0871, Japan. ²Innovative Technology Research Center, AGC Inc., 1150 Hazawa-cho, Kanagawa-ku, Yokohama, Kanagawa 221-8755, Japan. ³Materials and Life Science Division, J-PARC Center, Japan Atomic Energy Agency, Tokai, Ibaraki 319-1195, Japan. ⁴These authors contributed equally: Masahiko Okumura, Hiroki Nakamura, Mitsuhiro Itakura, Masahiko Machida, Shingo Urata and Kentaro Suzuya. [✉]email: kobayashi.keita@jaea.go.jp

(MD) simulations, and first-principles calculations based on the density functional theory (DFT), have been extensively used to obtain three-dimensional real-space structural information on disordered materials^{20,23,24,32–38}.

Over the past decade, a variety of machine learning techniques have been applied to predict material properties and characterize the structures of glasses^{39–44}. Specifically, machine learning molecular dynamics (MLMD) is a breakthrough in the accurate structural prediction of materials^{45–53}. In MLMD, flexible functions with several adjustable parameters are employed as interatomic potentials for MD simulations: for example, artificial neural networks^{45,46} and Gaussian processes^{47,48}. These are referred to as machine-learning potentials. Machine-learning potentials are trained with numerous DFT calculations to imitate the DFT potential-energy surface and enable large-scale MD simulations with near DFT accuracy. Machine-learning potentials for covalent glasses and liquids have been constructed using linear regression⁴⁹, artificial neural networks^{49–52}, and the Gaussian approximation potential⁵³. In particular, Erhard et al.⁵³ revealed that a machine-learning potential based on DFT with the strongly constrained and appropriately normed meta-GGA exchange-correlation functional⁵⁴ enabled high-accuracy calculations for various phases of silica. MLMD simulations, which can provide accurate real-space structural information with almost DFT accuracy, are expected to further our understanding of MRO in disordered materials.

In this study, we investigated the detailed microscopic structures as the origin of MRO in high-density silica glass using MLMD simulations with neural networks type machine-learning potential^{45,46} trained using the results of DFT calculations with the strongly constrained and appropriately normed meta-GGA exchange-correlation functional. We aimed to elucidate the relationship between the FSDP and the atomic structures of high-density silica glass. To achieve this outcome, we subjected silica glass to different types of deformations, as performed in previous experiments^{24,27,29,31}. We primarily focused on two types of high-density silica glass: silica glass under pressure (SGUP) at room temperature and densified silica glass created by hot compression (DSG). Elastic deformation is expected to dominate the deformation of the SGUP, whereas plastic deformation with Si–O bond recombination is expected to predominantly govern DSG formation. Investigating the difference in the deformation behavior between SGUP and DSG is expected to deepen our understanding of MRO in silica glass. We show that the MLMD simulations reasonably reproduce various experimental results for high-density silica glasses, including the enhancement (or reduction) of FSDP. The structural origin of MRO in the simulated high-density silica glasses was investigated from the perspective of the quasi-periodicity of the boundaries between successive cages formed by rings in the SiO_4 tetrahedral network. The difference between the structural origins of the MROs in the SGUP and DSG was clarified by examining the deformation manner of the rings under cold and hot compression.

Results

The structural properties of the ordinary silica glass (OSG) obtained via MLMD melt-quenching simulations are summarized in Table 1. The percentage error of the density in the experimental data was approximately 2.4 %, and the obtained bond lengths agreed well with the experimental results. The O–Si–O angle is extremely close to the central angle of the ideal tetrahedron, 109.47°. The Si–O–Si angle obtained through MLMD was comparable to the experimental data. Figure 1 shows the Faber–Ziman total structure factor $S_{\text{FZ}}(Q)$ of the simulated and experimental OSGs. Three distinctive peaks, Q_1 , Q_2 , and Q_3 , were observed for $S_{\text{FZ}}(Q)$. The first peak Q_1 is the FSDP, reflecting the MRO embedded in the SiO_4 tetrahedral networks. The second peak Q_2 is called as the principal peak (PP). The scale of the Q_2 agrees with the heights of the SiO_4 tetrahedra as $Q_2 \simeq 2\pi/(4d_{\text{SiO}}/3)$, and the PP is considered to reflect the local arrangement of the SiO_4 tetrahedra^{58,59}. The third peak Q_3 is a generic feature of amorphous materials arising from single-pairwise correlations between nearest-neighbor atoms^{23,59}. Although the total structure factor computed using MLMD slightly underestimates the height of the FSDP, all the peak positions of the $S_{\text{FZ}}(Q)$ show excellent agreement with the experimental data from low to high scattering vector Q . The structures of the simulated silica glass generated by MLMD simulations with near DFT accuracy were considered reliable for discussing the structural properties, including MRO.

Based on MLMD simulations, we analyzed the structural properties of two typical high-density silica glasses: SGUP and DSG. The pressure-density curve of the SGUP evaluated via MLMD was consistent with the trend of the experimental data, as shown in Fig. 2a. Figure 2b shows the density of the DSG created by compressing the OSG at various pressures and temperatures. Although the plastic deformation of silica glass at room temperature was experimentally observed at approximately 9 GPa^{60,61}, the density of the silica glass compressed at 10 GPa

	MLMD	Exp.
Density [g/cm ³]	2.245	2.196 ³⁵
d_{SiO} [Å]	1.61	1.61 ¹⁹
d_{SiSi} [Å]	3.08	3.07 ¹⁹
d_{OO} [Å]	2.62	2.62 ¹⁹
θ_{OSiO} [°]	109.41	109.47 ⁵⁶
θ_{SiOSi} [°]	144.57	148.3 ⁵⁶ , 146 ³²

Table 1. Structural properties of the OSG computed by MLMD. The Si–O, Si–Si, and O–O bond lengths (d_{SiO} , d_{SiSi} , and d_{OO}) are determined as the first-peak positions of pair-distribution functions. The averaged O–Si–O and Si–O–Si angles (θ_{OSiO} and θ_{SiOSi}) are defined using the mean value of the angle distributions.

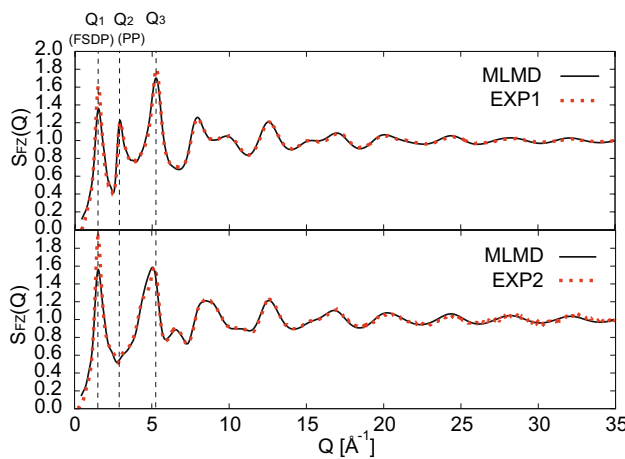


Figure 1. Faber-Ziman structure total factor $S_{FZ}(Q)$ of the OSG obtained via the MLMD melt-quenching simulation and experiment (Exp1²⁴ and Exp2⁵⁷). The upper and lower panels show the results of the ND and XRD, respectively.

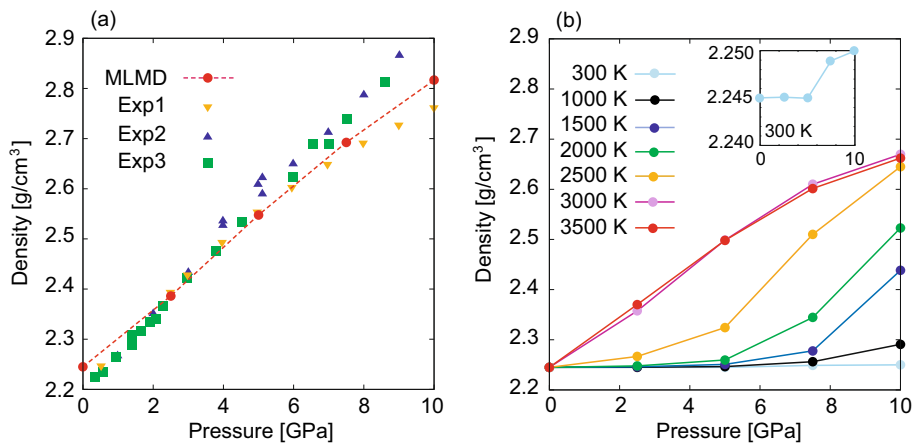


Figure 2. (a) Density change of the SGUP at 300 K. Circle dots denote the results obtained via MLMD. Square (Exp1), triangle (Exp2), and inverted triangle dots (Exp3) represent the experimental data^{60–62}. (b) Density of the DSGs compressed at different pressures and temperatures.

and 300 K was extremely low in the MLMD simulation (see the inset of Fig. 2b). This was due to the limitation of the time scale of the MD simulation, and compression at high temperatures was required to achieve a large structural relaxation of silica glass^{38,63–65}. On the timescale of the present simulation, densification due to hot compression above 1000 K can be detected. Sufficient structural relaxation of silica glass is considered to be realized above 3000 K, because the density of silica glass does not show a temperature dependence above 3000 K. Experimentally, silica glass can be densified up to approximately 23%, the value of which depends on the compression pressure and temperature^{24,28,30,66,67}. In the present simulation, with hot compression up to 10 GPa and 3500 K, the silica glass was densified by up to 19%.

Figure 3 shows the partial differential distribution $G_{\alpha\beta}(r)$ and angle distribution functions $P_{\alpha\beta\gamma}(\theta)$ of the OSG, the SGUP, and the DSG. The partial differential distribution function^{19,33} is defined as $G_{\alpha\beta}(r) = 4\pi\rho_0 r [g_{\alpha\beta}(r) - 1]$, where ρ_0 is the density of the silica glass. Herein, we focus on the SGUP and the DSG with almost the same density (2.692 and 2.662 [g/cm³], respectively). The first peak positions of $G_{OO}(r)$ and $G_{SiO}(r)$ in SGUP and DSG, which correspond to the O–O and Si–O bond lengths, were almost unchanged from those of OSG. All the peaks of the O–Si–O angle distribution functions are close to 109°, as shown in Fig. 3b. These results indicated that the structures of the SiO₄ tetrahedral units were well maintained under cold and hot compression. The peak of the Si–O–Si angle distribution of the SGUP largely shifted toward a lower angle than that of the OSG, whereas the corresponding peak shift of the DSG was small. In all cases, the contribution of the edge-sharing SiO₄ tetrahedra was negligible (see inset of Fig. 3e), and the SiO₄ networks of the glasses consisted of corner-sharing tetrahedral SiO₄. Overall, the peaks of $G_{\alpha\beta}(r)$ of the SGUP shifted to a lower position from those of the OSG, except the first peak. In addition, the ring size distribution of the SGUP was almost unchanged from that of the OSG, as shown in Fig. 4a. The structure of the SGUP is considered to have almost the same

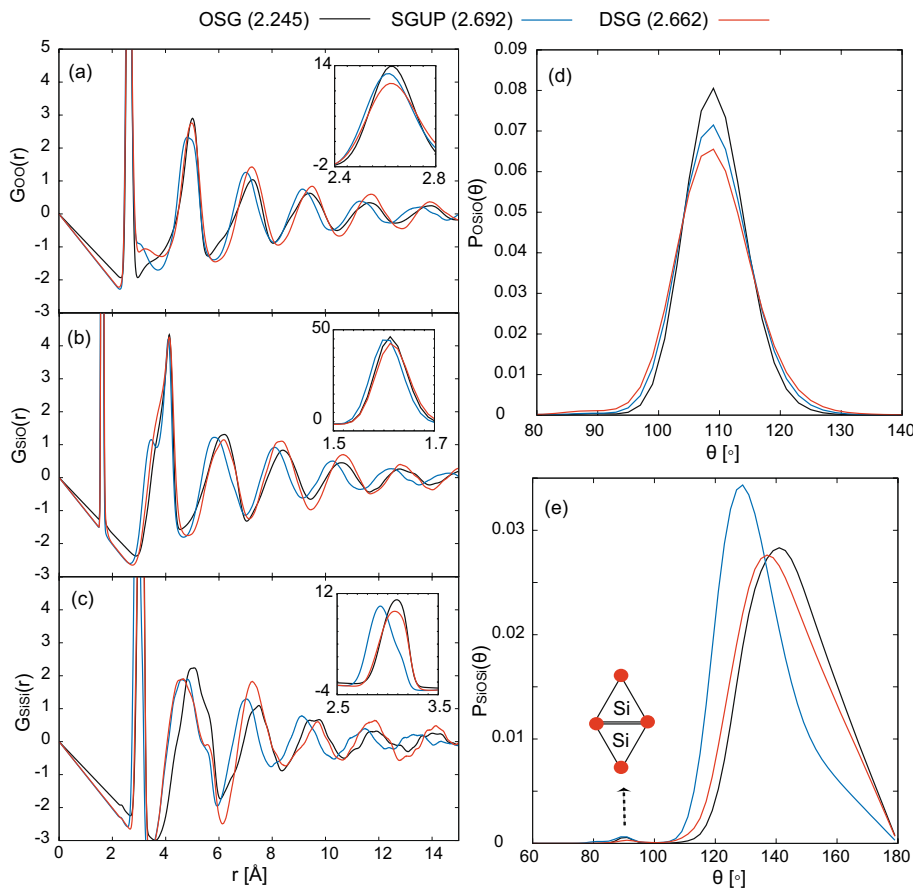


Figure 3. (a), (b), and (c): Partial differential distribution functions $G_{\alpha\beta}(r)$ for O-O, Si-Si, and Si-O pair. The insets show the first peak of $G_{\alpha\beta}(r)$. (d) and (e): O-Si-O and Si-O-Si angle distributions. The inset in (e) denotes the edge-sharing tetrahedron that contributes to the Si-O-Si angle distribution at approximately 90° . The distributions of OSG, SGUP, and DSG are indicated by the black, blue, and red lines, respectively. The values in (·) in the legends represent the density of the silica glass [g/cm^3].

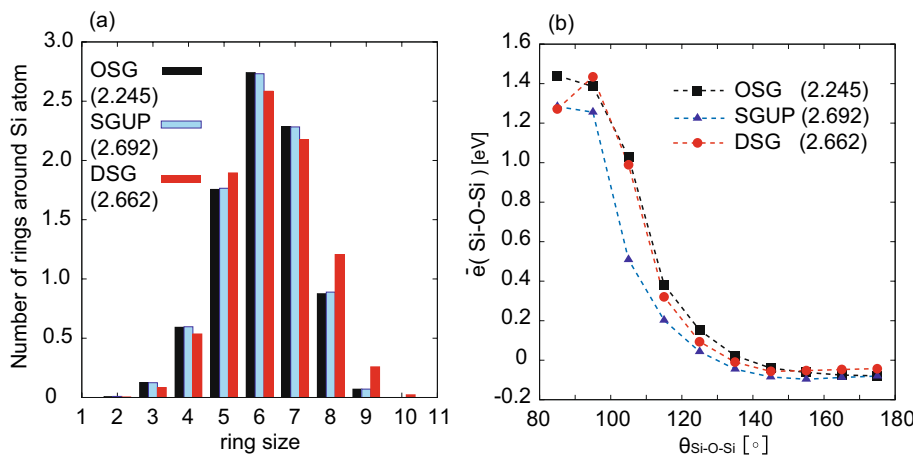


Figure 4. (a) Ring-size distribution around silicon atom for OSG, SGUP, and DSG. (b) Mean Si-O-Si atomic energy, $\bar{e}(\text{Si-O-Si})$ vs Si-O-Si angle, $\theta_{\text{Si-O-Si}}$. The Si-O-Si atomic energy is calculated from machine-learning potential atomic energy $e(i)$ as $\bar{e}(\text{Si-O-Si}) = \sum_{i \in \{\text{Si-O-Si}\}} (e(i) - \bar{e}(i))$, where $\bar{e}(i)$ is mean atomic energy of silicon and oxygen atoms. The values in (·) in the legends denote the density of silica glass [g/cm^3].

topology as that of the OSG with a reduced Si–O–Si angle. By contrast, in the case of the DSG, there is no regular trend with regard to the peak shifts of $G_{\alpha\beta}(r)$ from those of the OSG. Furthermore, the ratio of rings larger than seven-membered rings increased in the DSG compared to that in the OSG (see Fig. 4a). These results indicate that the structure of DSG has a different topology from those of OSG and SGUP because of the recombination of Si–O bonds by compression at high temperatures. The increase in the number of larger rings agrees with the reverse Monte Carlo result for the DSG created by hot compression²⁴. Notably, the creation of larger rings in the DSG is linked to a small change in the Si–O–Si angle distribution of the DSG (Fig. 3e). This is because large rings can adopt various configurations to allow large Si–O–Si angles, whereas the configurations of small rings are more constrained, and the deformation of small rings inevitably leads to a reduction in the Si–O–Si angle. From an energy perspective, a small Si–O–Si angle increases the local energy related to the Si–O–Si bond, as shown in Fig. 4b. Therefore, large rings were generated in the DSG to avoid the local energy increment owing to the significant reduction in the Si–O–Si angle caused by compression.

Figure 5a shows the Faber–Ziman total structure factors $S_{FZ}(Q)$ for SGUP and DSG with approximately the same density. The FSDP intensities of SGUP and DSG showed reduction and enhancement, respectively, which are in good agreement with previous experimental reports^{24,29,31} (see also Supplementary Information). In particular, MLMD successfully reproduced the enhancement of the FSDP in DSG, which was recently reported by Onodera et al.²⁴. The density dependence of the positions and heights of the FSDPs in the SGUP and DSGs compressed at various temperatures is shown in Fig. 5b. The positions of the FSDPs shifted towards a higher wavevector with increasing density in all cases, and the shifts of the DSGs were larger than those of the SGUP at almost the same density. Although the positions of the FSDP in the DSGs were slightly scattered, they were assumed to be proportional to the density, as observed in the experimental results²⁷. Regarding the density dependence of the height of the FSDP, although the height of the FSDP in the SGUP monotonically decreased with increasing density, those in the DSGs showed a reduction or enhancement depending on the compression temperature. As reported in the experiments, FSDP in DSG was sensitive to thermal treatment²⁴. The PPs in the $S_{FZ}(Q)$ observed by the ND became sharper with increasing density, which was considered to be related to the oxygen packing fraction^{23,58,59}. Although the PP usually does not appear in the XRD structure factor as in the case of the OSG and DSG, the $S_{FZ}(Q)$ observed via XRD for the SGUP reveals a small peak around 2.9 \AA^{-1} , which is also observed in in-situ high-pressure experiments³¹.

Discussion

We have demonstrated that the MLMD simulations accurately reproduced the experimental results for high-density silica glasses. Based on reliably simulated high-density silica glasses, we discuss the structural origin of the FSDP. The FSDP in silica glass has been considered to arise from the quasi-periodicity of the boundaries between successive cages formed by the rings in the SiO_4 tetrahedral network^{17–20}. To extract the quasi-periodicity of the boundaries from the simulated glasses, we evaluated the ring center pair distribution function defined as

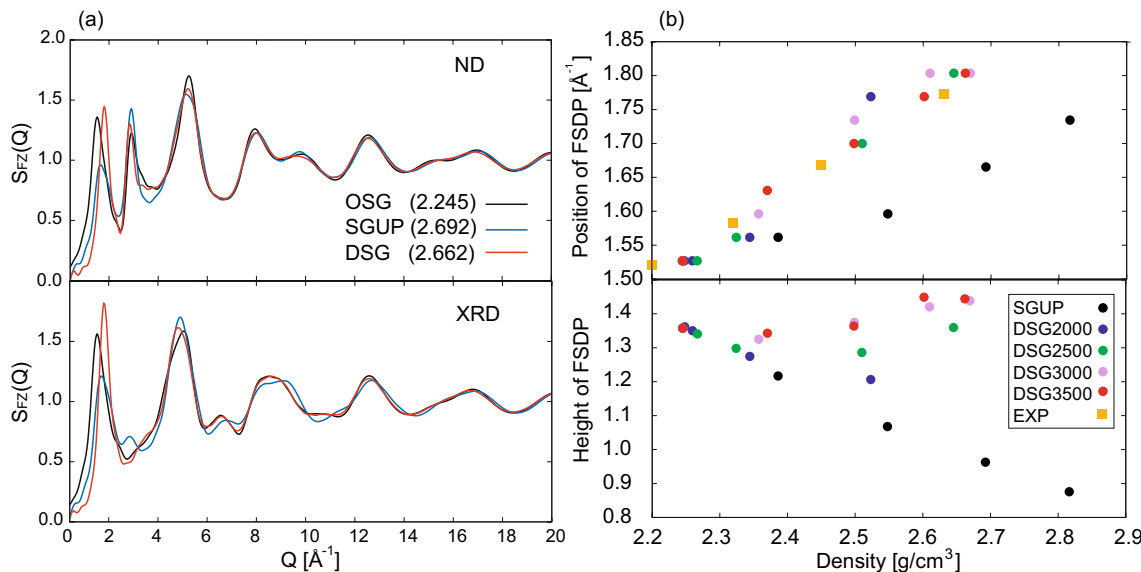


Figure 5. (a) Faber–Ziman total structure factor $S_{FZ}(Q)$ for ND and XRD computed via MLMD simulation. The black, blue, and red lines represent the structure factors for OSG, SGUP, and DSG, respectively. The values in (·) in the legends denote the density of silica glass [g/cm³]. (b) shows the density dependence of position (upper panel) and height (lower panel) of the FSDP in the Faber–Ziman structure factor of ND. The black dots denote the results of the SGUP. The blue, green, purple, and red dots represent the results of the DSGs compressed at 2000, 2500, 3000, and 3500 K (DSG2000, DSG2500, DSG3000, and DSG3500), respectively. The orange squares denote the experimental data of the DSG²⁷.

$$g_{RC}(r) = \sum_{i,j(\neq i)} \frac{V\delta(r - |\mathbf{r}_{RC,j} - \mathbf{r}_{RC,i}|)}{4\pi r^2 N_{RC}(N_{RC} - 1)}, \quad (1)$$

where V is the system volume, N_{RC} denotes the total number of the rings obtained by shortest path analysis, and $\mathbf{r}_{RC,i}$ indicates the centroid coordinate of i -th ring. Figure 6a shows the ring center differential distribution function, $G_{RC}(r) = 4\pi\rho_{RC}r[g_{RC}(r) - 1]$, where $\rho_{RC} = N_{RC}/V$. The peaks of $G_{RC}(r)$ in the short-range region within 3 Å are attributed to the overlapping of some centroid positions of the rings. The distinctive peaks appear in the intermediate range ($3 \text{ \AA} \leq r$) with a period $\Delta r \simeq 4$, which coincides with the scale of the FSDP, $Q_1 \simeq 2\pi/\Delta r$. We evaluated the ring center structure factor $S_{RC}(Q)$, defined by the Fourier transform of $g_{RC}(r)$, and the results are shown in Fig. 6b. The peak positions of $S_{RC}(Q)$ qualitatively reproduced the positions of the FSDPs in the total structure factor $S_{FZ}(Q)$. This result supports the conclusion of the previous studies that the origin of the FSDP is the quasi-periodicity between the succession of cages^{17–20}. Although the ring center structure factor $S_{RC}(Q)$ does not reproduce the change in the height of the FSDP in $S_{FZ}(Q)$, it can capture some characteristic features of the MRO in high-density silica glasses. The shapes of $S_{RC}(Q)$ for the OSG and SGUP are almost identical, and $S_{RC}(Q)$ for the SGUP is regarded as a simple shift of the OSG to a higher scattering vector, which is consistent with the trend of the partial differential distribution functions of the SGUP (see Fig. 3a–c). This result implies that the MRO in the SGUP and OSG are basically identical. By contrast, the peak of $S_{RC}(Q)$ of DSG is sharper than that of OSG and SGUP. The sharper peak indicates a clearer quasi-periodicity between the cage boundaries, which can also be confirmed by the long-lasting periodicity of $G_{RC}(r)$ of the DSG, as shown in Fig. 6a.

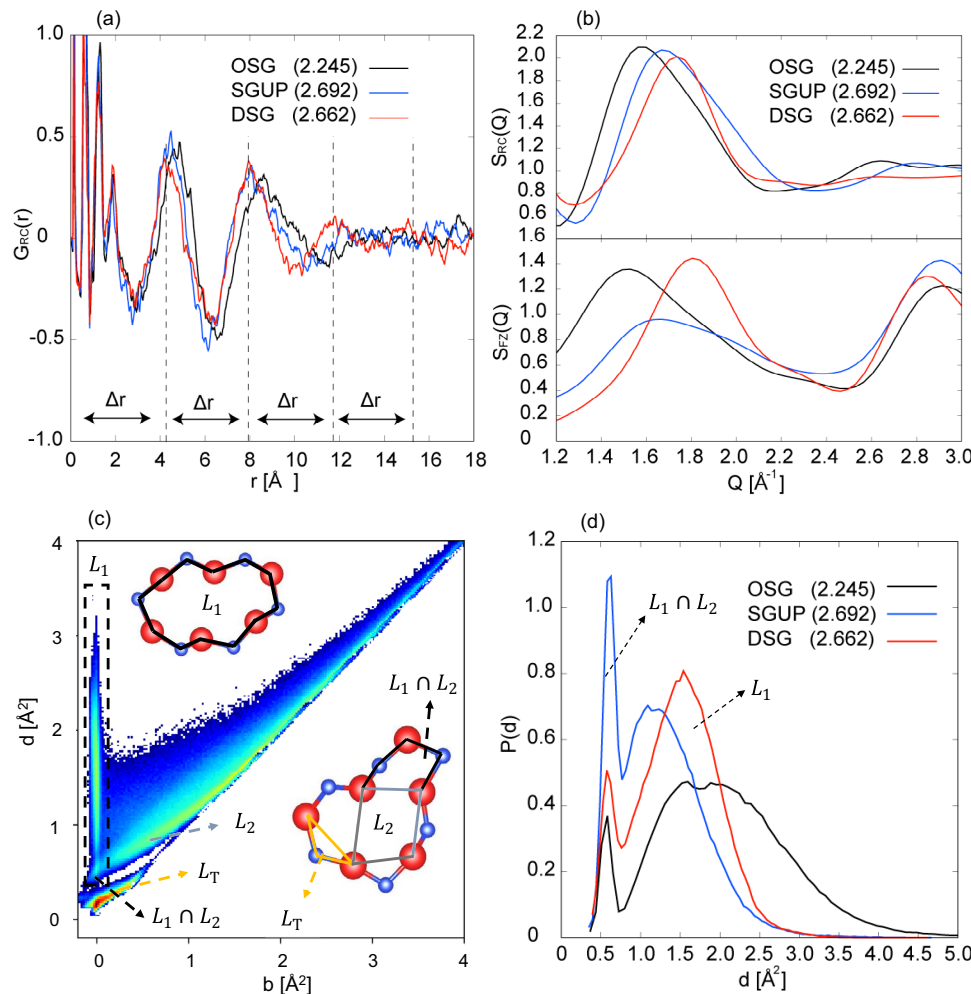


Figure 6. (a) Ring center differential distribution function $G_{RC}(r)$. (b) Upper panel shows the ring center structure factor and the lower panel represents the Faber–Ziman total structure factor of ND. (c) One-dimensional persistence diagram of the DSG with density 2.662 [g/cm³]. The horizontal and vertical axes (birth and death) represent the length scale of loops embedded in atomic configuration. (d) Probability distribution of death scale on the L_1 band (region enclosed by the black dashed line in (c)). The values in (·) in the legends denote the density of silica glass [g/cm³].

The ring center structure factor $S_{RC}(Q)$ does not reproduce the changes in the height of the FSDPs with increasing density because it only considers the correlation between ring centers and ignores information on the shapes of the rings. To address this issue, we used a persistence diagram to analyze the shapes of the rings in high-density silica glasses. Figure 6c shows the one-dimensional persistence diagram of the DSG with three characteristic bands: L_T , L_1 , and L_2 . The L_T band represents a triangular loop comprising silicon and its two nearest oxygen atoms, indicating a short-range order owing to the local structure of the SiO_4 tetrahedron (right lower panel in Fig. 6c). In the persistence diagram calculations, we defined the initial radii of the atomic balls for silicon r_{Si} and oxygen r_O to satisfy the condition $d_{\text{SiO}} = r_{\text{Si}} + r_O$. Therefore, the rings obtained through shortest path analysis based on Si–O bond length appear nearly on the vertical line along $b \simeq 0$ in the L_1 band (the left upper subpanel in Fig. 6c). The L_2 band represents the subloops arising within the loops in the L_1 band and continuing into the L_1 band. We refer to the intersecting region of the L_1 and L_2 bands as $L_1 \cap L_2$ band, which includes loops corresponding to largely distorted ring structures, as shown in the right lower panel of Fig. 6c. Figure 6d shows the probability distribution of the death scale for the L_1 band. Both the L_1 peaks of SGUP and DSG shift towards a smaller death scale, indicating that the mean ring radii are reduced in the high-density silica glasses. The primary difference between the SGUP and the DSG indicates the peak development related to the $L_1 \cap L_2$ band ($d \simeq 0.5$). In the SGUP, the peak of the $L_1 \cap L_2$ band significantly develops, and the boundary between the L_1 and the $L_1 \cap L_2$ bands is rendered ambiguous. This result suggests that compression causes extensive distortion of the ring shapes in the SGUP, which is consistent with the considerable reduction in the Si–O–Si angles illustrated in Fig. 3e. Consequently, the boundary surfaces of the cages formed by the rings in the SGUP are significantly disturbed compared to those in the OSG and DSG, which is considered to weaken the quasi-Bragg diffraction between the boundaries and decrease the FSDP. By contrast, the $L_1 \cap L_2$ peak of the DSG is small, and the L_1 peak becomes sharper. This indicates that structural relaxation accompanied by hot compression suppresses the creation of distorted rings caused by densification, resulting in more aligned boundary surfaces of successive cages in the DSG. The cage boundary surfaces of the DSG, which consist of rings with well-aligned length scales and small disturbances, enhance the quasi-Bragg diffraction related to the FSDP.

Finally, we uncover the underlying mechanism for developing the MRO, focusing on ring deformation caused by compression. We characterized deformation of the ring shape using a cuboid approximation of a ring on the ring pseudo-plane. To define the pseudo-plane for each ring, we computed the inertia tensor of the i -th ring as

$$M^{(i)} = \sum_{j \in i\text{-th ring}} \begin{pmatrix} y_j^2 + z_j^2 & -x_j y_j & -x_j z_j \\ -x_j y_j & x_j^2 + z_j^2 & -y_j z_j \\ -x_j z_j & -y_j z_j & x_j^2 + y_j^2 \end{pmatrix} \quad (2)$$

We then determined the axes of each ring's pseudo-plane using the principal axes of its inertia tensor. The lengths of the sides of the i -th ring approximated as a cuboid were defined as follows:

$$l_k^{(i)} = \max(\{[U^{(i)} \mathbf{r}_{j \in i\text{-th ring}}]_k\}) - \min(\{[U^{(i)} \mathbf{r}_{j \in i\text{-th ring}}]_k\}), \quad (3)$$

where $U^{(i)}$ is the matrix to diagonalize $M^{(i)}$ and the index k denotes the principal axes of the inertia tensor ($k = 1, 2, 3$). The ordering of $l_k^{(i)}$ is such that $l_1^{(i)} \leq l_2^{(i)} \leq l_3^{(i)}$, where $l_1^{(i)}$ represents the thickness of the pseudo-plane of the i -th ring, l_2 and l_3 characterize the shape of the ring within the pseudo-plane (see Fig. 7a), respectively. To quantify the deformation of the ring shape, we evaluated the average aspect ratio of the sides, l_2/l_3 , of the cuboids approximating the ring shapes. The aspect ratio, l_2/l_3 , indicates the shape of a ring in the pseudo-plane, where a value close to 1 suggests that the shape of the ring is close to isotropic in the pseudo-plane, whereas a small value of l_2/l_3 indicates that the ring has an elongated shape. The aspect ratio, l_2/l_3 , revealed noteworthy differences between the shapes of the rings in the SGUP and DSG (see Fig. 7b). For small rings, the l_2/l_3 of the SGUP decreased from that of the OSG, while the ratios of the DSG and OSG were almost identical. This difference between SGUP and DSG indicates that cold compression deforms the small rings, whereas hot compression retains the shape of the small rings. By contrast, for large rings, l_2/l_3 of the DSG is smaller than that of the SGUP—the rings in the DSG are more deformed than those in the SGUP. The difference in ring deformation between SGUP and DSG was attributed to the presence or absence of Si–O bond recombination. Because Si–O bond recombination is absent in the SGUP, all rings are forcefully deformed with a significant reduction in the Si–O–Si angles (Fig. 3e), and the ring shapes are distorted (Figs. 6d, 7c). By contrast, the Si–O bond recombination in the DSG through hot compression suppressed the considerable reduction in the Si–O–Si angles and the distorted shape of the rings by preferentially deforming the large rings. This is because large rings can adopt various configurations to allow large Si–O–Si angles, as discussed previously. The large structural relaxation caused by hot compression deforms the large rings into elongated shapes and retains the shape of the small rings, as shown in Fig. 7c, preventing a local energy increase resulting from small Si–O–Si angles (see Fig. 4b).

The primary contribution to the formation of the FSDP is thought to originate from the length scale of l_2 , since the l_2 distribution contains primarily the length scale of the FSDP, $Q_1 = 2\pi/\Delta r = 1.5 \sim 1.8$, where $\Delta r \simeq 3.5 \sim 4.2$ (see Figs. 5, 7d). By examining the l_2 distributions of the ring sizes, we elucidated the relationship between ring deformation and the change in MRO in high-density silica glass. The l_2 distributions of the SGUP exhibited almost uniform shifts toward a smaller length scale compared to those of the OSG, as shown in Fig. 7e. The differences in the length scales between the different ring sizes of the SGUP were similar to those of the OSG, indicating that the quasi-periodicity of the cage boundaries was basically identical to that of the OSG. This result agrees with the analysis of the partial differential distribution functions and ring center structure factor of the SGUP. By contrast, the distributions of the smaller rings of the DSG than 5-member are almost unchanged compared to those of the OSG, whereas those of the larger rings than 7-member largely shifted to a small length

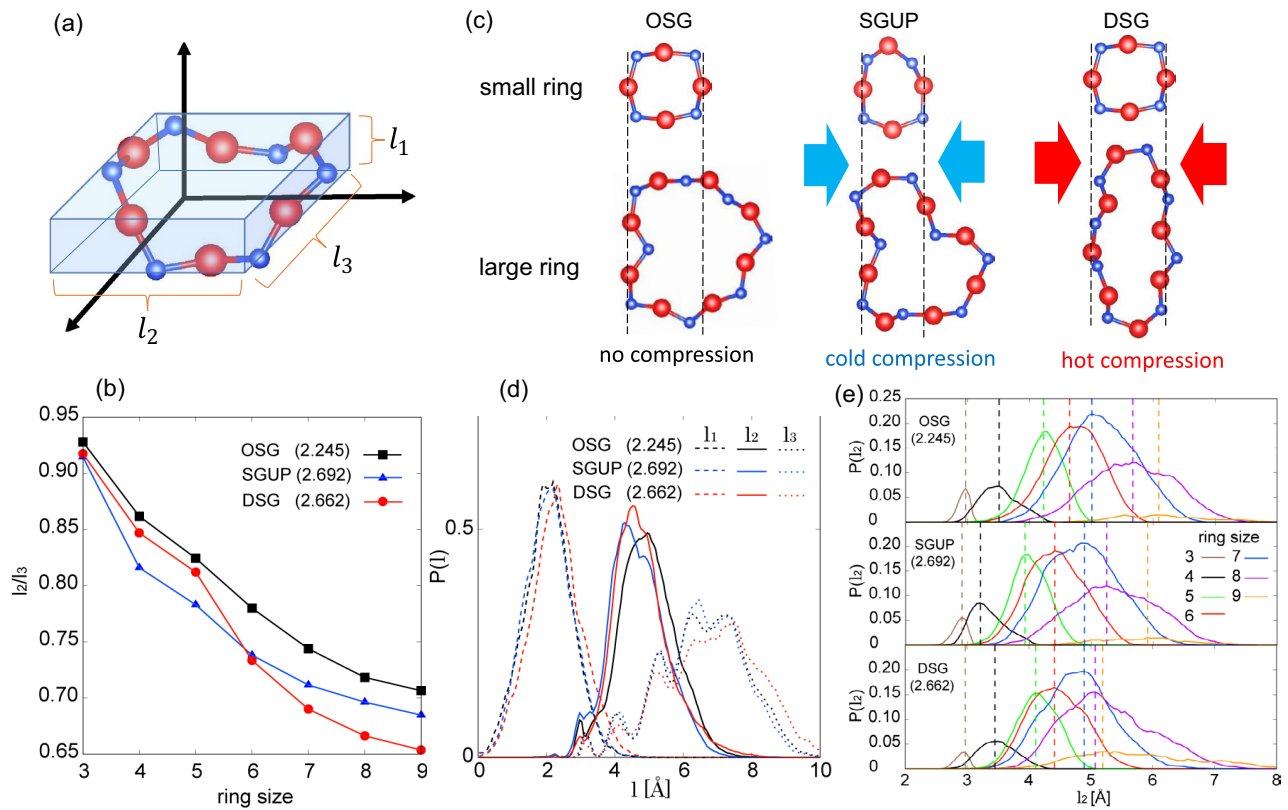


Figure 7. (a) Ring approximated as a cuboid on the principal axes of the moment tensor of a ring. l_1 , l_2 , and l_3 represent the length of the sides of the cuboid ($l_1 \leq l_2 \leq l_3$). (b) Averaged ratio of the sides of the cuboid l_2/l_3 for each ring size. (c) Schematic figures of ring deformation for small and large rings of SGUP and DSG. (d) Distribution of l_1 , l_2 , and l_3 for OSG, SGUP and DSG. (e) Distribution of l_2 calculated for each ring size. Dashed lines represent the peak position of the l_2 distribution for guide. The values in (·) in the legends denote the density of silica glass [g/cm^3].

scale from those of the OSG. Thus, the l_2 distributions of the rings of the DSG exhibit a large overlap compared to those of the SGUP and OSG, indicating the aligned length scales of rings with different sizes (see also the schematic figure of the DSG in Fig. 7c). The aligned length scales of the rings in the DSG are directly linked to the deformation of the rings in the DSG, i.e., small rings in the DSG tend to maintain their shape, whereas large rings tend to become elongated. Consequently, the length scales (l_2) of the different rings are rendered close, and the aligned length scales of the rings enhance the quasi-periodicity of the SiO_4 network in the DSG.

Conclusion

We have performed extensive MLMD simulations to explore the structural origin of MRO in high-density silica glass. Our MLMD simulation reasonably reproduced the structural properties of high-density silica glasses observed in experiments, including the reduction and enhancement of the FSDP depending on the compression temperature. Based on the structures of the simulated high-density silica glasses, we investigated the structural origin of the difference in the FSDPs between SGUP and DSG, which have almost the same density. Two primary factors were identified that influence the reduction or development of the FSDP in these high-density silica glasses. The first relates to the shape of boundary surfaces of cages formed by rings, quantifiable through persistent diagrams. The second factor is associated with the quasi-periodicity in the SiO_4 tetrahedral network, which correlates with the length scale of the rings. Under cold compression for the SGUP, there was no recombination of the Si–O bond, meaning that the topology of the SiO_4 tetrahedral network remains unchanged. This observation was supported by the partial differential distribution, ring statistics, and the ring center pair distribution function. The reduction in FSDP within the SGUP is attributed to the ring shape distortion caused by compression, which in turn weakens the quasi-Bragg diffraction between the boundary surfaces of successive cages in the SiO_4 tetrahedral network. For the DSG created by hot compression, the recombination of the Si–O bond created and deformed large rings. The creation and deformation of the large rings occurred in order to avoid a local energy increase associated with a significant reduction of the Si–O–Si angles by densification. This is because large rings have flexibility, allowing for larger Si–O–Si angles in a high-density state, whereas the deformation of smaller rings inevitably results in a reduction of the Si–O–Si angles. The large rings tended to deform into elongated shapes, characterized by significant changes in their aspect ratios (l_2/l_3), while the shape of smaller rings remains almost unchanged. Consequently, the length scales of small to large rings (l_2) became close, and quasi-periodicity developed. The large structural relaxation through high-temperature compression

caused the cage boundary surfaces to form rings with well-aligned length scales and small distortions, which contributed to the enhancement of the FSDP.

Methods

Machine learning molecular dynamics

A machine-learning potential based on the Behler-Parrinello type neural network^{45,46} was created using the n2p2 code. The details and validations of the proposed machine-learning potential are provided in the Supplementary Information. MD simulations with the machine-learning potential were performed using the LAMMPS code⁶⁸ with an n2p2 interface. A Nosè-Hoover thermostat^{69,70} and a Parrinello-Rahman barostat^{71,72} were used to control the temperature and pressure of the systems, respectively.

Simulated silica glass

Ordinary silica glass (OSG) structures were created via melt quenching simulations. We first conducted an *NPT* simulation of liquid silica with 1728 atoms at 3500 K. The time step and total simulation time were 1 fs and 500 ps, respectively. Five configurations of liquid silica were selected at 100 ps intervals from the MD trajectories. A melt-quenching simulation was then performed for the five structures from temperatures of 3500–300 K at a cooling rate of 0.5 K/ps. In this study, we calculated all the physical quantities of simulated silica glasses from MD trajectories generated via *NPT* simulations with 100 ps run at 300 K. In addition, we assumed the ensemble average using five different configurations of silica glass to improve the statistical certainty of the physical quantities.

We also created two types of simulated high-density silica glass: SGUP and DSG. The SGUPs were prepared by applying various pressures (2.5, 5.0, 7.5, and 10 GPa) to the simulated OSG with a simulation time of 100 ps at 300 K. The DSGs were created by compressing the simulated OSG at high temperatures (1000, 1500, 2000, 2500, 3000, and 3500 K) and pressures (2.5, 5.0, 7.5, and 10 GPa). The OSG was compressed at the target pressure and temperature for 100 ps, and then cooled to 300 K at a rate of 0.5 K/ps. After the quenching simulation, the applied pressure was gradually released to 0 GPa for 100 ps. The physical properties of the simulated high-density silica glasses were computed in the same manner as those for the OSG.

Faber-Ziman total structure factor

We calculated the Faber-Ziman total structure factor from the partial pair distribution function $g_{\alpha\beta}(r)$ of the simulated silica glass as

$$S_{FZ}(Q) = \sum_{\alpha, \beta} \frac{c_{\alpha} c_{\beta} b_{\alpha}(Q) b_{\beta}(Q)}{\langle b(Q) \rangle^2} S_{\alpha\beta}(Q), \quad (4)$$

$$S_{\alpha\beta}(Q) = 1 + 4\pi\rho_0 \int dr r^2 \frac{\sin(Qr)}{Qr} (g_{\alpha\beta}(r) - 1), \quad (5)$$

where ρ_0 is the density of the silica glass, c_{α} is the concentration of chemical species ($\alpha = \text{Si}, \text{O}$), and $b_{\alpha}(Q)$ is the neutron (or X-ray) scattering factor for the chemical species, and $\langle b(Q) \rangle$ denotes the average of the scattering factor as $\langle b(Q) \rangle \equiv \sum_{\alpha} c_{\alpha} b_{\alpha}(Q)$. We used neutron scattering lengths, $b_{\text{Si}} = 4.1491$ and $b_{\text{O}} = 5.803$, to calculate the total structure factor of the ND. The Q-dependent scattering factors $b_{\alpha=\text{Si}, \text{O}}(Q)$ for the calculation of the total structure factor of the XRD were taken from the reference⁷³.

Topological analysis

The topology embedded in the SiO_4 network in high-density silica glass was analyzed using ring statistics and persistence homology analyses^{21,74}. The ring size distribution was computed using shortest path analysis⁷⁵. We defined the edges of an undirected graph from the Si–O bonds and collected the shortest rings connected to an Si atom using a depth-first search. Persistence homology analysis was performed using the HomCloud package⁷⁴. The mathematical details of persistence homology can be found in the references^{21,74}. In this method, we generate an atomic ball with radius $r_i(\alpha) = \sqrt{\alpha + r_i^2}$, where r_i is the initial radius of each atom and the parameter α is an adjustable parameter. By varying α from zero to a sufficiently large value, we can detect the loops embedded in the atomic configuration at each α . The detected loops are characterized by birth and death scales (b and d), at which the loop first appears ($\alpha^2 = b$) and disappears ($\alpha^2 = d$). Subsequently, the persistence diagram is given as a 2D histogram counting the number of loops on the birth-death plane, which provides quantitative information on both the shape and length of the loops embedded in the SiO_4 network. In this study, the input radii of oxygen and silicon atoms (r_{O} and r_{Si}) were determined from the O–O and Si–O bond lengths (d_{OO} and d_{SiO}) as $r_{\text{O}} = d_{\text{OO}}/2$ and $r_{\text{Si}} = d_{\text{SiO}} - r_{\text{O}}$ ²¹.

Data availability

The machine learning potentials and the datasets generated during the current study are available from the corresponding author on reasonable request.

Received: 24 August 2023; Accepted: 11 October 2023

Published online: 16 November 2023

References

- Pun, A. K., Siddhartha, & Singh, A. K. Thermo-mechanical and erosion wear peculiarity of hybrid composites filled with micro and nano silicon dioxide fillers—A comparative study. *Silicon* **11**, 1885–1901 (2019).
- Palumbo, F. *et al.* A review on dielectric breakdown in thin dielectrics: Silicon dioxide, high-k, and layered dielectrics. *Adv. Funct. Mater.* **30**, 1900657. <https://doi.org/10.1002/adfm.201900657> (2020).
- Devine, R. A. *The Physics and Technology of Amorphous SiO₂* (Springer Science, 2012).
- Elliott, S. R. Medium-range structural order in covalent amorphous solids. *Nature* **354**, 445–452. <https://doi.org/10.1038/354445a0> (1991).
- Gaskell, P. H. & Wallis, D. J. Medium-range order in silica, the canonical network glass. *Phys. Rev. Lett.* **76**, 66–69. <https://doi.org/10.1103/PhysRevLett.76.66> (1996).
- Christie, J. K., Taraskin, S. N. & Elliott, S. R. Structural characteristics of positionally disordered lattices: Relation to the first sharp diffraction peak in glasses. *Phys. Rev. B* **70**, 134207. <https://doi.org/10.1103/PhysRevB.70.134207> (2004).
- Phillips, J. Topology of covalent non-crystalline solids II: Medium-range order in chalcogenide alloys and $A - Si(Ge)$. *J. Non-Cryst. Solids* **43**, 37–77. [https://doi.org/10.1016/0022-3093\(81\)90172-1](https://doi.org/10.1016/0022-3093(81)90172-1) (1981).
- Busse, L. E. & Nagel, S. R. Temperature dependence of the structure factor of as_2Se_3 glass up to the glass transition. *Phys. Rev. Lett.* **47**, 1848–1851. <https://doi.org/10.1103/PhysRevLett.47.1848> (1981).
- Wright, A. C., Sinclair, R. N. & Leadbetter, A. J. Effect of preparation method on the structure of amorphous solids in the system As-S. *J. Non-Cryst. Solids* **71**, 295–302. [https://doi.org/10.1016/0022-3093\(85\)90299-6](https://doi.org/10.1016/0022-3093(85)90299-6) (1985) (Effects of Modes of Formation on the Structure of Glass).
- Cervinka, L. Medium-range order in amorphous materials. *J. Non-Cryst. Solids* **106**, 291–300. [https://doi.org/10.1016/0022-3093\(88\)90277-3](https://doi.org/10.1016/0022-3093(88)90277-3) (1988).
- Blétry, J. Sphere and distance models for binary disordered systems. *Philos. Mag. B* **62**, 469–508. <https://doi.org/10.1080/13642819008215248> (1990).
- Elliott, S. R. Origin of the first sharp diffraction peak in the structure factor of covalent glasses. *Phys. Rev. Lett.* **67**, 711–714. <https://doi.org/10.1103/PhysRevLett.67.711> (1991).
- Kawasaki, T., Araki, T. & Tanaka, H. Correlation between dynamic heterogeneity and medium-range order in two-dimensional glass-forming liquids. *Phys. Rev. Lett.* **99**, 215701 (2007).
- Tah, I., Sengupta, S., Sastry, S., Dasgupta, C. & Karmakar, S. Glass transition in supercooled liquids with medium-range crystalline order. *Phys. Rev. Lett.* **121**, 085703 (2018).
- Kohara, S. *et al.* Relationship between diffraction peak, network topology, and amorphous-forming ability in silicon and silica. *Sci. Rep.* **11**, 22180 (2021).
- Shi, Y. *et al.* Revealing the relationship between liquid fragility and medium-range order in silicate glasses. *Nat. Commun.* **14**, 13 (2023).
- Zachariasen, W. H. The atomic arrangement in glass. *J. Am. Chem. Soc.* **54**, 3841–3851 (1932).
- Greaves, G. Exafs and the structure of glass. *J. Non-Cryst. Solids* **71**, 203–217. [https://doi.org/10.1016/0022-3093\(85\)90289-3](https://doi.org/10.1016/0022-3093(85)90289-3) (1985) (Effects of Modes of Formation on the Structure of Glass).
- Mei, Q., Benmore, C. J., Sen, S., Sharma, R. & Yarger, J. L. Intermediate range order in vitreous silica from a partial structure factor analysis. *Phys. Rev. B* **78**, 144204. <https://doi.org/10.1103/PhysRevB.78.144204> (2008).
- Kohara, S. *et al.* Atomic and electronic structures of an extremely fragile liquid. *Nat. Commun.* **5**, 5892. <https://doi.org/10.1038/ncomms6892> (2014).
- Hiraoka, Y. *et al.* Hierarchical structures of amorphous solids characterized by persistent homology. *Proc. Natl. Acad. Sci.* **113**, 7035–7040. <https://doi.org/10.1073/pnas.1520877113> (2016).
- Shi, Y. *et al.* Ring size distribution in silicate glasses revealed by neutron scattering first sharp diffraction peak analysis. *J. Non-Cryst. Solids* **516**, 71–81. <https://doi.org/10.1016/j.jnoncrysol.2019.03.037> (2019).
- Onodera, Y. *et al.* Understanding diffraction patterns of glassy, liquid and amorphous materials via persistent homology analyses. *J. Ceram. Soc. Jpn.* **127**, 853–863. <https://doi.org/10.2109/jcersj2.19143> (2019).
- Onodera, Y. *et al.* Structure and properties of densified silica glass: Characterizing the order within disorder. *NPG Asia Mater.* **12**, 85. <https://doi.org/10.1038/s41427-020-00262-z> (2020).
- Sørensen, S. S., Biscio, C. A. N., Bauchy, M., Fajstrup, L. & Smedskjaer, M. M. Revealing hidden medium-range order in amorphous materials using topological data analysis. *Sci. Adv.* **6**, eabc2320. <https://doi.org/10.1126/sciadv.abc2320> (2020).
- Zhou, Q., Shi, Y., Deng, B., Neufeind, J. & Bauchy, M. Experimental method to quantify the ring size distribution in silicate glasses and simulation validation thereof. *Sci. Adv.* **7**, eabh1761. <https://doi.org/10.1126/sciadv.ahb1761> (2021).
- Inamura, Y. *et al.* Intermediate range structure and low-energy dynamics of densified vitreous silica. *J. Non-Cryst. Solids* **293–295**, 389–393. [https://doi.org/10.1016/S0022-3093\(01\)00824-9](https://doi.org/10.1016/S0022-3093(01)00824-9) (2001) (8th Int. Conf. on Non-Crystalline Materials).
- Wakabayashi, D., Funamori, N., Sato, T. & Taniguchi, T. Compression behavior of densified SiO₂ glass. *Phys. Rev. B* **84**, 144103. <https://doi.org/10.1103/PhysRevB.84.144103> (2011).
- Zeidler, A. *et al.* High-pressure transformation of SiO₂ glass from a tetrahedral to an octahedral network: A joint approach using neutron diffraction and molecular dynamics. *Phys. Rev. Lett.* **113**, 135501. <https://doi.org/10.1103/PhysRevLett.113.135501> (2014).
- Masuno, A. *et al.* Higher refractive index and lower wavelength dispersion of siO₂ glass by structural ordering evolution via densification at a higher temperature. *RSC Adv.* **6**, 19144–19149. <https://doi.org/10.1039/C5RA25106K> (2016).
- Kono, Y. *et al.* Experimental evidence of tetrahedral symmetry breaking in SiO₂ glass under pressure. *Nat. Commun.* <https://doi.org/10.1038/s41467-022-30028-w> (2022).
- Kohara, S. & Suzuya, K. Intermediate-range order in vitreous SiO₂ and GeO₂. *J. Phys.: Condens. Matter* **17**, S77–S86. <https://doi.org/10.1088/0953-8984/17/5/009> (2005).
- Vashishta, P., Kalia, R. K., Rino, J. & Ebbsjö, I. Interaction potential for SiO₂: A molecular-dynamics study of structural correlations. *Phys. Rev. B* **41**, 12197–12209. <https://doi.org/10.1103/PhysRevB.41.12197> (1990).
- Rino, J., Ebbsjö, I., Kalia, R. K., Nakano, A. & Vashishta, P. Structure of rings in vitreous SiO₂. *Phys. Rev. B* **47**, 3053–3062. <https://doi.org/10.1103/PhysRevB.47.3053> (1993).
- Sarnthein, J., Pasquarello, A. & Car, R. Structural and electronic properties of liquid and amorphous SiO₂: An ab initio molecular dynamics study. *Phys. Rev. Lett.* **74**, 4682–4685. <https://doi.org/10.1103/PhysRevLett.74.4682> (1995).
- Sarnthein, J., Pasquarello, A. & Car, R. Model of vitreous SiO₂ generated by an ab initio molecular-dynamics quench from the melt. *Phys. Rev. B* **52**, 12690–12695. <https://doi.org/10.1103/PhysRevB.52.12690> (1995).
- Massobrio, C. & Pasquarello, A. Origin of the first sharp diffraction peak in the structure factor of disordered network-forming systems: Layers or voids?. *J. Chem. Phys.* **114**, 7976–7979. <https://doi.org/10.1063/1.1365108> (2001).
- Ryu, E., Wakabayashi, D., Koura, A. & Shimojo, F. Ab initio simulation of permanent densification in silica glass. *Phys. Rev. B* **96**, 054206. <https://doi.org/10.1103/PhysRevB.96.054206> (2017).
- Cubuk, E. D. *et al.* Identifying structural flow defects in disordered solids using machine-learning methods. *Phys. Rev. Lett.* **114**, 108001 (2015).
- Yang, K. *et al.* Predicting the young's modulus of silicate glasses using high-throughput molecular dynamics simulations and machine learning. *Sci. Rep.* **9**, 8739 (2019).

41. Cubuk, E. D., Liu, A. J., Kaxiras, E. & Schoenholz, S. S. *Unifying framework for strong and fragile liquids via machine learning: a study of liquid silica* **2008**, 09681 (2020).
42. Bødker, M. L., Bauchy, M., Du, T., Mauro, J. C. & Smedskjaer, M. M. Predicting glass structure by physics-informed machine learning. *npj Comput. Mater.* **8**, 192 (2022).
43. Tah, I., Ridout, S. A. & Liu, A. J. Fragility in glassy liquids: A structural approach based on machine learning. *J. Chem. Phys.* **157**, 124501. <https://doi.org/10.1063/5.0099071> (2022).
44. Shiba, H., Hanai, M., Suzumura, T. & Shimokawabe, T. Botan: Bond targeting network for prediction of slow glassy dynamics by machine learning relative motion. *J. Chem. Phys.* **158**, 084503. <https://doi.org/10.1063/5.0129791> (2023).
45. Behler, J. & Parrinello, M. Generalized neural-network representation of high-dimensional potential-energy surfaces. *Phys. Rev. Lett.* **98**, 146401. <https://doi.org/10.1103/PhysRevLett.98.146401> (2007).
46. Behler, J. Constructing high-dimensional neural network potentials: A tutorial review. *Int. J. Quantum Chem.* **115**, 1032–1050 (2015).
47. Bartók, A. P., Payne, M. C., Kondor, R. & Csányi, G. Gaussian approximation potentials: The accuracy of quantum mechanics, without the electrons. *Phys. Rev. Lett.* **104**, 136403. <https://doi.org/10.1103/PhysRevLett.104.136403> (2010).
48. Bartók, A. P. & Csányi, G. Gaussian approximation potentials: A brief tutorial introduction. *Int. J. Quantum Chem.* **115**, 1051–1057 (2015).
49. Li, W. & Ando, Y. Comparison of different machine learning models for the prediction of forces in copper and silicon dioxide. *Phys. Chem. Chem. Phys.* **20**, 30006–30020. <https://doi.org/10.1039/c8cp04508a> (2018).
50. Balyakin, I. A., Rempel, S. V., Ryltsev, R. E. & Rempel, A. A. Deep machine learning interatomic potential for liquid silica. *Phys. Rev. E* **102**, 052125. <https://doi.org/10.1103/PhysRevE.102.052125> (2020).
51. Kobayashi, K., Nagai, Y., Itakura, M. & Shiga, M. Self-learning hybrid Monte Carlo method for isothermal-isobaric ensemble: Application to liquid silica. *J. Chem. Phys.* **155**, 034106. <https://doi.org/10.1063/5.0055341> (2021).
52. Urata, S. *et al.* Suppression of rayleigh scattering in silica glass by codoping boron and fluorine: Molecular dynamics simulations with force-matching and neural network potentials. *J. Phys. Chem. C* **126**, 2264–2275 (2022).
53. Erhard, L. C., Rohrer, J., Albe, K. & Deringer, V. L. A machine-learned interatomic potential for silica and its relation to empirical models. *npj Comput. Mater.* **8**, 90. <https://doi.org/10.1038/s41524-022-00768-w> (2022).
54. Sun, J., Ruzsinszky, A. & Perdew, J. P. Strongly constrained and appropriately normed semilocal density functional. *Phys. Rev. Lett.* **115**, 036402 (2015).
55. Handbook, C. *CRC Handbook of Chemistry and Physics* 88th edn. (CRC Press, 2007).
56. Neufeind, J. & Liss, K.-D. Bond angle distribution in amorphous Germania and silica. *Ber. Bunsenges. Phys. Chem.* **100**, 1341–1349. <https://doi.org/10.1002/bbpc.19961000812> (1996).
57. Ohara, K., Onodera, Y., Murakami, M. & Kohara, S. Structure of disordered materials under ambient to extreme conditions revealed by synchrotron x-ray diffraction techniques at spring-8–recent instrumentation and synergic collaboration with modelling and topological analyses. *J. Phys.: Condens. Matter* **33**, 383001. <https://doi.org/10.1088/1361-648X/ac0193> (2021).
58. Kono, Y. & Sanloup, C. *Magmas Under Pressure: Advances in High-Pressure Experiments on Structure and Properties of Melts* (Elsevier, 2018).
59. Salmon, P. S. & Zeidler, A. Ordering on different length scales in liquid and amorphous materials. *J. Stat. Mech: Theory Exp.* **2019**, 114006. <https://doi.org/10.1088/1742-5468/ab3cce> (2019).
60. Meade, C. & Jeanloz, R. Frequency-dependent equation of state of fused silica to 10 GPa. *Phys. Rev. B* **35**, 236–244. <https://doi.org/10.1103/PhysRevB.35.236> (1987).
61. Tsiok, O. B., Brazhkin, V. V., Lyapin, A. G. & Khvostantsev, L. G. Logarithmic kinetics of the amorphous–amorphous transformations in SiO₂ and GeO₂ glasses under high pressure. *Phys. Rev. Lett.* **80**, 999–1002. <https://doi.org/10.1103/PhysRevLett.80.999> (1998).
62. Bridgman, P. W. The compression of 39 substances to 100,000 kg/cm. *Proc. Am. Acad. Arts Sci.* **76**, 55–70 (1948).
63. Jin, W., Kalia, R. K., Vashishta, P. & Rino, J. P. Structural transformation, intermediate-range order, and dynamical behavior of SiO₂ glass at high pressures. *Phys. Rev. Lett.* **71**, 3146–3149. <https://doi.org/10.1103/PhysRevLett.71.3146> (1993).
64. Huang, L. & Kieffer, J. Amorphous–amorphous transitions in silica glass. II. Irreversible transitions and densification limit. *Phys. Rev. B* **69**, 224204. <https://doi.org/10.1103/PhysRevB.69.224204> (2004).
65. Yang, Y., Homma, O., Urata, S., Ono, M. & Mauro, J. C. Topological pruning enables ultra-low Rayleigh scattering in pressure-quenched silica glass. *npj Comput. Mater.* **6**, 1–8 (2020).
66. MACKENZIE, J. D. High-pressure effects on oxide glasses: I, densification in rigid state. *J. Am. Ceram. Soc.* **46**, 461–470. <https://doi.org/10.1111/j.1151-2916.1963.tb13776.x> (1963).
67. Arndt, D. & Stöffler, J. Anomalous changes in some properties of silica glass densified at very high pressures. *Phys. Chem. Glass.* **10** (1969).
68. Plimpton, S. Fast parallel algorithms for short-range molecular dynamics. *J. Comput. Phys.* **117**, 1–19 (1995).
69. Nosé, S. A unified formulation of the constant temperature molecular dynamics methods. *J. Chem. Phys.* **81**, 511–519 (1984).
70. Hoover, W. G. Canonical dynamics: Equilibrium phase-space distributions. *Phys. Rev. A* **31**, 1695 (1985).
71. Parrinello, M. & Rahman, A. Crystal structure and pair potentials: A molecular-dynamics study. *Phys. Rev. Lett.* **45**, 1196 (1980).
72. Parrinello, M. & Rahman, A. Polymorphic transitions in single crystals: A new molecular dynamics method. *J. Appl. Phys.* **52**, 7182–7190 (1981).
73. Waasmaier, D. & Kirfel, A. New analytical scattering actor functions for free atoms and ions. *Acta Crystallogr. A* **51**, 416–431. <https://doi.org/10.1107/S0108767394013292> (1995).
74. Obayashi, I., Nakamura, T. & Hiraoka, Y. Persistent homology analysis for materials research and persistent homology software: Homcloud. *J. Phys. Soc. Jpn.* **91**, 091013. <https://doi.org/10.7566/JPSJ.91.091013> (2022).
75. KING, S. V. Ring configurations in a random network model of vitreous silica. *Nature* **213**, 1112–1113. <https://doi.org/10.1038/2131112a0> (1967).
76. Momma, K. & Izumi, F. Vesta: A three-dimensional visualization system for electronic and structural analysis. *J. Appl. Crystallogr.* **41**, 653–658 (2008).

Acknowledgements

This calculations were mainly performed on the supercomputing system HPE SGI8600 in the Japan Atomic Energy Agency. We would thank all staff members of CCSE for computational support. We also used the computational resources of Fujitsu PRIMERGY CX400M1/CX2550M5 (Oakbridge-CX), Fujitsu PRIMEHPC FX1000, FUJITSU PRIMERGY GX2570 (Wisteria/BDEC-01), and “mdx: a platform for the data-driven future” supported by “Joint Usage/Research Center for Interdisciplinary Large-scale Information Infrastructures” in Japan (Project ID: jh230069). H.N. was partially supported by JSPS KAKENHI Grants No. 23K04637. The crystal structures were drawn with VESTA⁷⁶.

Author contributions

K.K. performed the simulations and drafted the manuscript; M.O., H.N., M.I., M.M., S.U., and K.S. improved the idea and the manuscript. All authors have reviewed and approved the final manuscript.

Competing interests

The authors declare no competing interests.

Additional information

Supplementary Information The online version contains supplementary material available at <https://doi.org/10.1038/s41598-023-44732-0>.

Correspondence and requests for materials should be addressed to K.K.

Reprints and permissions information is available at www.nature.com/reprints.

Publisher's note Springer Nature remains neutral with regard to jurisdictional claims in published maps and institutional affiliations.



Open Access This article is licensed under a Creative Commons Attribution 4.0 International License, which permits use, sharing, adaptation, distribution and reproduction in any medium or format, as long as you give appropriate credit to the original author(s) and the source, provide a link to the Creative Commons licence, and indicate if changes were made. The images or other third party material in this article are included in the article's Creative Commons licence, unless indicated otherwise in a credit line to the material. If material is not included in the article's Creative Commons licence and your intended use is not permitted by statutory regulation or exceeds the permitted use, you will need to obtain permission directly from the copyright holder. To view a copy of this licence, visit <http://creativecommons.org/licenses/by/4.0/>.

© The Author(s) 2023